Laser-guided corrosion control: a new approach to tailor the degradation of Mg-alloys

Pablo Pou-Álvarez, Antonio Riveiro, Xosé Ramón Nóvoa, Xueze Jin, Jesús del Val, Rafael Comesaña, Mohamed Boutinguiza, Fernando Lusquiños, Julian R. Jones, María Teresa Pérez-Prado, and Juan Pou**

P. Pou-Álvarez, Dr. J. del Val, Dr. M. Boutinguiza, Dr. F. Lusquiños, Prof. J. Pou
Applied Physics Department, University of Vigo, E.E.I., Lagoas-Marcosende, Vigo, 36310, Spain.

Dr. A. Riveiro, Dr. R. Comesaña
Materials Engineering, Applied Mechanics and Construction Department, University of Vigo, E.E.I., Lagoas-Marcosende, Vigo, 36310, Spain.

Prof. X. R. Nóvoa
ENCOMAT group, University of Vigo, E.E.I., Lagoas-Marcosende, Vigo, 36310, Spain.

X. Jin, Dr. M.T. Pérez-Prado
IMDEA Materials Institute, C/ Eric Kandel, 2, Getafe, Madrid 28906, Spain.

P. Pou-Álvarez, Prof. J.R. Jones
Department of Materials, Imperial College London, South Kensington Campus, London, SW7 2AZ, UK.

Dr. M. Boutinguiza, Dr. F. Lusquiños, Prof. J. Pou
Galicia Sur Health Research Institute (IIS Galicia Sur). SERGAS - University of Vigo, Vigo, Spain.

*Corresponding authors. Email: ariveiro@uvigo.es, jpou@uvigo.es

Keywords: laser, corrosion, biodegradation, magnesium, guided corrosion, corrosion control

Abstract:

Despite corrosion is commonly seen as a problem to be avoided, applications as batteries or biodegradable implants do benefit from corrosion-like phenomena. However, current strategies address corrosion control from a global perspective for a whole component, without considering local adaptations to functionality specifications or inhomogeneous environments. Here, a novel concept is presented: the local control and guidance of corrosion through a laser surface treatment. Immersion tests in saline solution of AZ31 magnesium alloy samples show degradation rates reduced up to 15 times with the treatment, owing to a fast passivation after the induced microstructural modifications. By controlling the treatment conditions, the degradation can be restricted to delimited regions and driven towards specific directions. The

applicability of the method for the design of tailored degradation biomedical implants is demonstrated and uses for cathodic protection systems and batteries can also be anticipated.

Main Text:

Corrosion has been a challenging engineering problem for centuries in many fields, as linked to the loss of the functionality of the corroded components arise serious personal, environmental and economic risks. However, certain applications do benefit from corrosion-like phenomena, as batteries,[1,2] cathodic protection systems[3,4] or biodegradable implants.[5–7] In those fields, corrosion must not be avoided, but instead proceed in a controlled manner.

Current strategies for corrosion control include a variety of bulk and surface processing approaches adapted to different materials and applications. A common characteristic for all these approaches is that corrosion control is generally addressed from a global perspective for the whole component.[8–10] However, functionality specifications or inhomogeneous environmental conditions may require a local control of the corrosion rate in different regions of a component.

Particularly, in biodegradable implants used for biomedical applications, the material is intended to be dissolved by corrosion in contact with the body fluids after supplying the required mechanical support or delivery of drugs. There, differences in healing times of the host tissue and variations in body fluids flow rate and composition around different areas of the implant do demand a local control of the corrosion process.[5–7]

This work explores the feasibility of guiding the corrosion of a target component towards specific regions and directions by means of a laser-based surface treatment technique. Through a local control of the key surface properties governing the corrosion phenomena, the corrosion rate in each predefined region of the component could be selectively adjusted. The overall corrosion process would then be guided by the laser treatment and become predictable and controllable. This new concept of “laser-guided corrosion control” has not yet been explored to the best of the authors’ knowledge.

To implement this idea, the usually employed AZ31 magnesium alloy (3% Al, 1% Zn, 0.6 % Mn, see Experimental Section and Table S1) was selected. On the basis of the naturally occurring corrosion of magnesium in contact with body fluids and its high biocompatibility, magnesium is commonly utilized for the development of biodegradable implants for orthopedic and cardiovascular applications.[11–13] However, the *in vivo* degradation of magnesium is often unpredictable and too fast, involving problems as premature degradation, environment alkalinisation and hydrogen accumulation, which restricts its wider use.[11–15]

Laser surface treatments have been employed to increase the corrosion resistance of magnesium and its alloys, mostly based on microstructural changes after melting and resolidification processes.[16,17] Here, the material was treated with nanosecond pulsed laser irradiation. Under this processing regime, metals usually undergo local melting and evaporation, with thermal effects normally extended to a micrometric depth at most, due to the short interaction times.[18] Through the control of two galvo mirrors the laser beam was easily focused with an F-Theta lens on the required sites of the material surface. Specifically, the material was irradiated following a pattern of parallel scanning lines (see Experimental Section). As displayed in **Figure 1**a, a groove pattern is formed on the flat surface of the base material during the treatment. Along each scanning line, the material under the incident laser radiation is melted and displaced sideways by the so-called recoil pressure, generated by momentum conservation during the expansion of the metal vapor at the center of the irradiated spot.[19,20]

This groove formation with the treatment resulted in a general increase of the surface roughness, with values depending on the processing parameters employed. Taking roughness measurements as a first assessment of the extent of surface modification, 2 levels of pulse fluence F, i.e. average single pulse energy per area (1.8 and 0.7 J cm^{-2}), and 2 levels of scanning speed v (10 and 60 mm s^{-1}) were selected, giving a set of 4 main treatments. The final S_a roughness range from (1.6 ± 0.2) µm for the base material (i.e. untreated) to (29 ± 3) µm for T1 treatment, as quantified by optical profilometry (see Experimental Section and Table S2).

The extent of improvement of the corrosion performance with the laser treatment was then explored by immersion tests (see Experimental Section) in normal saline solution of both base material and treated samples (11 × 11 × 1 mm^3). Figure 1b shows a series of optical microscopy images of the different samples after each incubation time. It is clear that the base material experiences severe degradation, which leads to almost complete dissolution after 14 days of immersion. In contrast, degradation is drastically reduced for the laser-treated samples. Indeed, the integrity of T1 sample is maintained for the whole duration of the test, owing to its slower corrosion. As shown, the performance of the processed samples is clearly dependent on the employed processing parameters, with T2, T3 and T4 samples showing an intermediate behavior between the performance of T1 and base material samples.

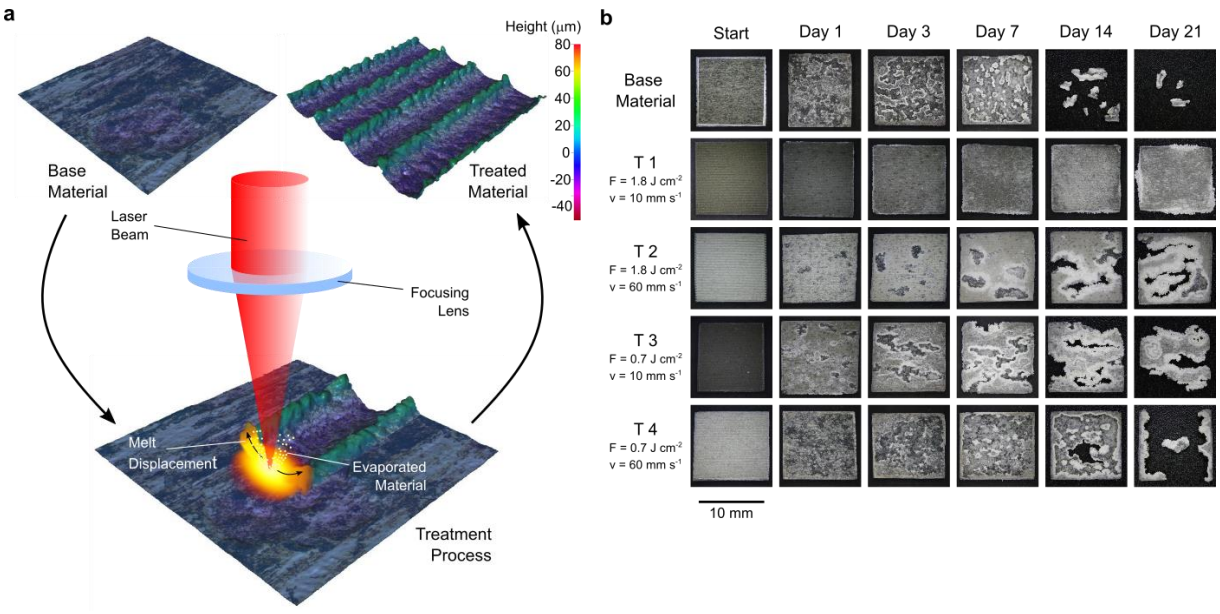

Figure 1. Laser treatment and overall corrosion behavior. a) Optical profilometry images with height map for the untreated base material and a representative treated sample, with a representation of the treatment process. b) Optical images of macroscopic appearance of base material and differently-treated samples (T1 -T4) after specific immersion times in the NaCl solution.

In the corrosion process of magnesium in aqueous solutions, magnesium atoms from the metal surface are oxidized to magnesium ions and water molecules are reduced to hydrogen and hydroxide ions according to Equation (1):[21–23]

$$Mg_{(s)} + 2H_2O \rightarrow Mg^{2+}_{(aq)} + 2OH^-_{(aq)} + H_{2(g)} \quad (1)$$

Magnesium and hydroxide ions precipitate as magnesium hydroxide $Mg(OH)_2$ for *pH* values above 10.35 (solubility product constant $K_{sp} = 5.6 \times 10^{-12}$ at 25 °C)[24], providing a moderate protection against corrosion. In the presence of chloride ions, the formation of magnesium chloride ($MgCl_2$) is thermodynamically favored due to its much higher solubility (558 g l^{-1} in water at 25 °C)[24]. That prevents the stabilization of $Mg(OH)_2$ protective layer and, consequently, a high net rate of metallic Mg dissolution is established.

On this basis, to quantify the degradation of the immersed samples, mass loss, Mg^{2+} released and *pH* increase with OH^- release were measured (see Experimental Section). As illustrated in Figure S1, the three measurements verify the degradation trends macroscopically observed (Figure 1b). The degradation rates estimated from the mass loss within the first 14 days of immersion range from (35 ± 2) mg dm^{-2} day^{-1} for T1-treated material to (530 ± 10) mg dm^{-2} day^{-1} for the base material (Figure S1b). This means that the laser treatment can reduce the corrosion rate by a factor of approximately 15, thereby drastically improving the base material behavior. Furthermore, by tuning the processing parameters, the degradation rate can be modulated, gradually increasing from T1 to T4.

Due to the roughness increase, the actual exposed surface area in the treated samples is higher than in the base material. This difference amounts to a factor of approximately 4 for T1 treatment, according to the profilometry measurements (see Experimental Section). Besides, wettability measurements (see Experimental Section) revealed a hydrophilic behavior for the base material, with a contact angle $\theta = (50 \pm 10)°$ (see Figure S2). The wettability increased with the laser treatment up to a superhydrophilic regime ($\theta = 0°$ for T1 treatment), with the water filling the generated grooves by capillary wicking.[25,26] This also occurs when samples are immersed in solution, so the observed trends in corrosion performance are not explained by alterations of the solid/liquid contact area, which actually increases with the treatment.

To investigate further the evident differences between the untreated and treated samples, the corrosion process during immersion was monitored in real time with a video camera (see

Experimental Section and Supplementary Video 1). For the base material the corrosion starts locally, with several dispersed sites showing slight hydrogen evolution during the first minutes. The extension and intensity of corrosion increases with time, with vigorous hydrogen evolution from 1 hour onward and evident macroscopic degradation after a few hours. In contrast, for the T1-treated material, the corrosion starts homogeneously over the entire surface with substantial hydrogen evolution from the beginning. However, within just 5 minutes, this behavior is reduced almost entirely. Therefore the treated material appears to be able to go through a homogeneous passivation process, after which the corrosion is drastically reduced compared to the base material.

The corrosion mechanism of both treated and untreated samples was then studied in detail via electrochemical impedance spectroscopy (EIS, see Experimental Section). EIS data collected immediately following sample stabilization in the solution and the fitted equivalent circuit are presented in **Figure 2**a-c.

For the base material (Figure 2a), a capacitive loop around 100 Hz - 1 kHz can be distinguished. This loop is related to the electrochemical dissolution of magnesium at sites where metal is exposed and can be modeled by a charge transfer resistance R_{CT} and a double-layer capacitance C_{DL}.[27] In addition, at low frequencies, about 1 Hz, an inductive loop can be observed. This loop is linked to the existence of adsorbed intermediate species, such as Mg^{+}, which facilitate the corrosion kinetics at active dissolution sites of the sample[28,29] and was modeled by an inductance L with a series resistance R_L.[30]

For the T1-treated sample (Figure 2b), the loop around 100 Hz - 1 kHz associated with magnesium dissolution can also be identified. However, much higher R_{CT} (Base Mat: 29.9 Ω cm^2, T1: 319.9 Ω cm^2) and lower C_{DL} values (Base Mat: 42.8 μF cm^{-2}, T1: 1.2 μF cm^{-2}) were found. In addition, a second capacitive loop around 10 Hz is also present. This loop was modeled by a finite-length diffusion impedance Z_D (see Experimental Section), linked to ion

transport processes between the reaction sites and the bulk solution.[27,28] The absence of the inductive loop at low frequencies is also notable.

The growth of a protective non-metallic surface layer with a passivation process for the treated material can explain all those differences. The presence of such a layer can easily reduce the total metal/solution contact area and therefore the number of active dissolution sites, accounting for the higher R_{CT}, the lower C_{DL} and for the absence of the low frequency inductive behavior for the treated material.[28,31] Additionally, this layer can also restrict ion diffusion, introducing the diffusion impedance term, almost negligible in the case of the base material (Base Mat: 3.6 Ω cm^2, T1: 322.1 Ω cm^2). The high frequency end of the spectrum above 10 kHz for the treated material (see inset in Figure 2b) shows another capacitive feature, which can in fact be modeled by the properties of a dielectric layer[32,33] (i.e resistance R_F and capacitance C_F) and thus also reinforces the passivation hypothesis. The overall measured corrosion resistance of the treated material is substantially higher than that of the base material (polarization resistance for Base Mat: 16 Ω cm^2, T1: 672 Ω cm^2, see Experimental Section and Figure S3a,c) and increased over time, indicating the progress of the passivation process.[27,28]

To confirm the existence of a protective layer and explain its formation, both base material and treated samples were examined in cross-section before and after immersion in the NaCl solution. A scanning electron microscopy (SEM) backscattered electron (BSE) representative image of a cross-section of non-immersed base material is shown in Figure 2d. A homogeneous Mg matrix and dispersed Al-Mn-Fe micro-particles with diameters reaching approximately 10 µm can be distinguished, as confirmed by energy-dispersive X-ray spectroscopy (EDS) maps (see Figure S4a) and in agreement with common observations for Al-Mn-containing Mg-alloys.[34] Figure 2g shows an electron backscatter diffraction (EBSD, see Experimental Section) inverse pole figure (IPF) map of a cross section of the base material. The appearance of hexagonal close-packed (HCP) α-Mg grains was confirmed, with a mean size of 7.45 µm and typically ranging within (2.38, 11.95) µm. A defined basal crystallographic texture, with basal planes

preferentially parallel to the sample surface, was found as shown. This texture is typical of hot rolled Mg-alloy, as the one used here (see Experimental Section), and develops as a consequence of plastic deformation through basal slip during forming followed by recrystallization.[35,36]

Figure 2e,f show SEM BSE representative images for non-immersed T1-treated material. The bulk microstructure is similar to that of the base material and, therefore, was not modified by the laser treatment. However, a recast layer (i.e. melted and resolidified) approximately 10 μm thick can be identified at the surface of the sample (Figure 2f). The Al-Mn-Fe particles that are present in the untreated material seem to have been dissolved into the melt according to EDS maps (see Figure S4a). As a consequence of this redissolution, a statistically significant increase in the (Al+Mn)/Mg atomic ratio in the Mg solid solution was detected (two-sided Kolmogorov-Smirnov test, p-value = 2.6×10^{-4}), from 0.020 ± 0.001 for the base material to 0.025 ± 0.006 within the recast layer. No significant grain boundary segregation was detected within the recast layer, and only a few dispersed Al-Mn rich nanometric precipitates were apparent. Furthermore, as shown by EBSD image (Figure 2h), the microstructure was refined within this layer, with a mean grain size of 1.43 μm and typically ranging within (0.27, 2.45) μm. As seen in Figure 2h, during solidification there was preferential grain growth following the heat flow towards the bulk material (grain size aspect ratio approximately 2.4). In addition, the refined grains exhibit a random texture, in contrast to the relatively strong texture of the base material. The fast cooling rates achieved by the laser treatment, which can reach 10^{11} K s^{-1} for nanosecond pulse processing,[20] explain both the grain refinement, due to the increase of the nucleation rate during solidification, and the retention of the alloying elements within the solid solution, as a consequence of the short diffusion times allowed.[16,17,37,38]

Figure 2j shows the appearance of a corrosion site in a base material sample after immersion in NaCl solution for 16 hours. The accumulation of an irregular and thick layer of corrosion products is clearly visible. An O/Mg atomic ratio of 2.1 ± 0.3 was found in EDS analysis,

indicating the presence of $Mg(OH)_2$ as the main component of the layer, as expected. The layer presents clear pores and cracks, allowing the electrolyte to access the bare metallic surface, so that corrosion can progress further. In contrast, the surface of the treated material is barely corroded (Figure 2k). At a higher magnification (Figure 2l), a thin corrosion products layer approximately 1 μm thick can be distinguished. Compared to that of the base material, the layer is more uniform and compact and, hence, able to provide an effective overall protection against solution penetration. The lower O/Mg atomic ratio of 0.9 ± 0.4 found is consistent with a decreased layer hydration degree. Comparison of O distribution from EDS mappings of Figure 2j and Figure 2l reinforces this point (see Figure S4b).

The improved corrosion resistance of the treated samples can be mainly explained in terms of the recast layer microstructure. The appearance of Al-Mn-Fe particles in the base material is detrimental for the corrosion resistance of the alloy, as those sites can act as local cathodes accelerating the dissolution rate of the more anodic matrix by galvanic coupling.[21,39] In contrast, the redissolution of the alloying elements with the laser treatment would reduce these galvanic coupling effects.[17,37,38,40] This protection mechanism is further supported by consistent results of improved corrosion behavior after treatment obtained in experiments with AZ61 and AZ91 Mg-alloys. As well, the extent of protection measured in experiments with pure magnesium was not enough to prevent its complete dissolution after a few hours, presumably due to the fact that its corrosion does not arise from galvanic coupling with secondary phases but from a much lower corrosion resistance of the Mg matrix itself (see Table S1 and Figure S5). In addition, as precipitation is feasible in the immersion conditions, the grain refinement achieved would help to passivate the material, as a more dense network of reactive grain boundaries can ease the stabilization of a protective oxides/hydroxides layer.[16,41] Additionally, the slight increase of the amount of alloying elements within the solid solution in the recast layer can also play a moderate but still beneficial role by formation of more corrosion resistant protective film compounds.[21,42] The crystallographic orientation would not play an

important role in the corrosion resistance in this case, as the random orientation of the grains within the recast layer would be in any case detrimental compared to the basal orientation of grains exposed by the base material (the basal plane is the most densely packed plane and thus the one with higher corrosion resistance).[36] Additional experiments comparing treatments in air and argon atmospheres revealed also a moderate role in corrosion resistance played by oxidation during the treatment as characterized by XPS analyses (see Experimental Section), which adds an extra protection to that arising from the microstructure modifications (Figure S6).

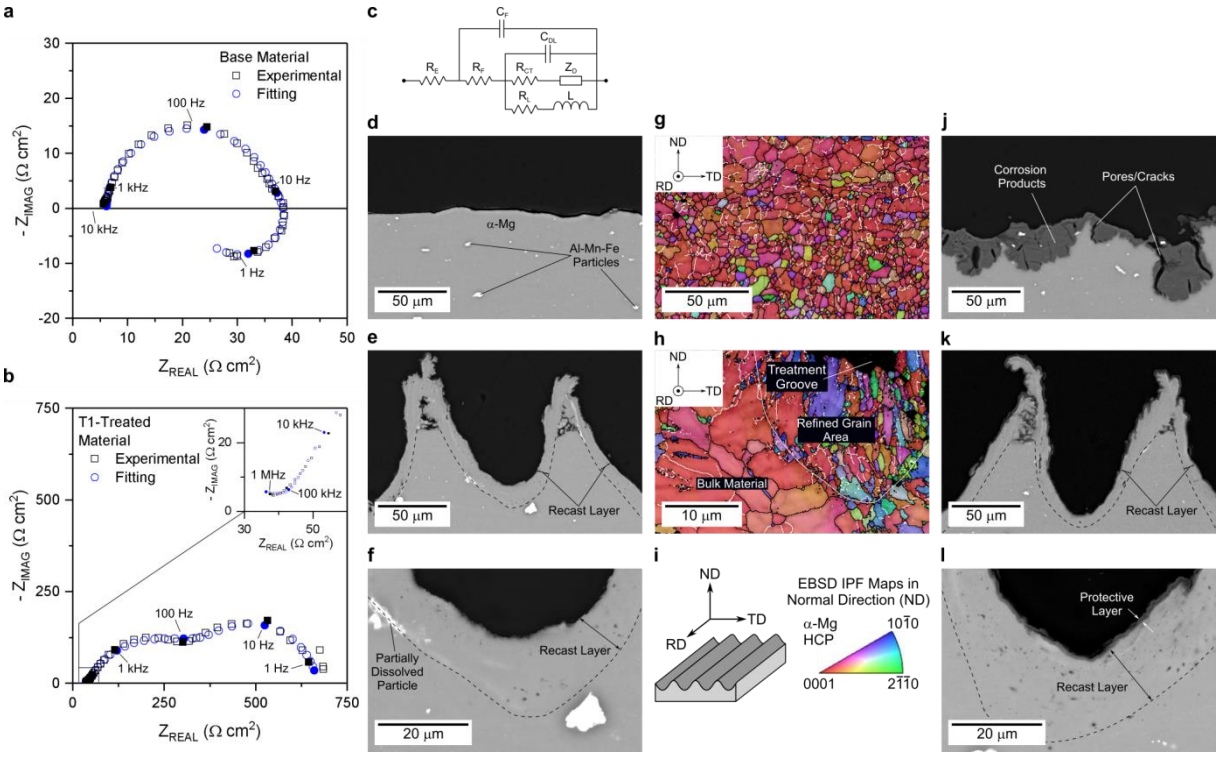

Figure 2. Electrochemical and microstructural characterization. a-c) EIS data for base material (a) and T1-treated material (b) recorded immediately following stabilization in the NaCl solution, along with the corresponding equivalent circuit (c). Here, R_E represents the electrolyte resistance. All other circuit elements are described in the main text (see Experimental Section for further description). Fitted values are included in Figure S3c. d-f) SEM BSE images of a cross-section of non-immersed base material (d), T1-treated sample (e) and a higher magnification image of the latter (f), where a partially dissolved Al-Mn-Fe particle on the edge of the recast layer can be appreciated. g-i) EBSD IPF maps in the normal direction (ND) for base material (g) and T1-treated material (h). See legend (i), where RD and TD stand for rolling and transverse directions respectively. j-l) SEM BSE images in cross-section after 16 hours of immersion in the NaCl solution. A thick but porous/cracked and non-protective layer of corrosion products can be seen for the base material (j), while a thinner, compact and protective layer is apparent for the treated material (k, l). Dashed lines indicate the limit of the recast layer in panels (e, f, h, k and l).

Based on the protective properties of the recast layer generated by the laser treatment, the role of the processing parameters can be discussed. A clear relation was found between the pulse

fluence and the width of the generated grooves (T1 versus T3, T2 versus T4 in Figure S7). That means that the lateral displacement of the molten material increased for higher fluence. For a laser spot with Gaussian irradiance (i.e. power density) distribution, this trend can be explained by an increase of the actual area of the spot with sufficient irradiance to achieve melting and evaporation, as well as higher overall recoil pressure levels over the liquid when the fluence is increased.[19,43] As the recast layer is able to passivate during immersion, in terms of corrosion performance, logically, the fraction of the surface covered by this layer plays a major role, which explains the observed effects of pulse fluence in the immersion tests results (T1 versus T3, T2 versus T4 in Figure 1b). In fact, an inductive behavior was detected in the EIS measurements for T3 sample (Figure S3b), explained by the presence of uncovered regions (i.e. untreated base material) due to the lower pulse fluence employed.

Besides, the depth of the grooves and the thickness of the recast layer were found to depend mainly on the scanning speed (T1 versus T2, T3 versus T4 in Figure S7). When the scanning speed is reduced, the number of pulses irradiated per unit area is increased. As the thermal relaxation time (approximately 10^{-4} s, see Experimental Section) is longer than the period between pulses (5×10^{-5} s), the surface is still hot when a new pulse arrives. Therefore, the spatial accumulation of pulses results in an increase of the heat penetration via conduction and, consequently, of the amount of molten material. Then, the higher irradiance levels in the center of the Gaussian profile lead to preferential displacement/ejection of material from deeper rather than wider locations as the pulse sequence irradiates the surface.[44] With regard to the degradation performance, even if all the surface is covered by a protective layer, relatively thicker layers of recast material are preferable, as they would provide improved self-repairing ability if corrosion starts at any eventual defect or irregularity of the layer. This can explain the observed corrosion trends for varying scanning speed (T1 versus T2, T3 versus T4 in Figure 1b).

Once the corrosion protection mechanism induced by the laser treatment has been identified and controlled, different possibilities of corrosion guidance can be explored. The corrosion/degradation can be restricted to delimited regions of interest by an easy control of the treated areas to be protected. **Figure 3**b serves as proof of this concept. As indicated, a defined area of the sample was treated, leaving both the center and the corners untreated. As shown, corrosion starts selectively in the untreated regions, and advances macroscopically, dissolving all the material until it reaches a treated area (refer to Supplementary Video 2 for video version). Furthermore, the corrosion rate of each region can be selectively adjusted by controlling the treatment parameters, as previously discussed. On this basis, for example, gradual treatments can be applied to achieve a directional control of the degradation. Figure 3c shows how a vertical gradual treatment is able to induce a gradual advance of the degradation in the same direction. Therefore, rates, areas and directions of the corrosion advance can be controlled, so that the process becomes predictable.

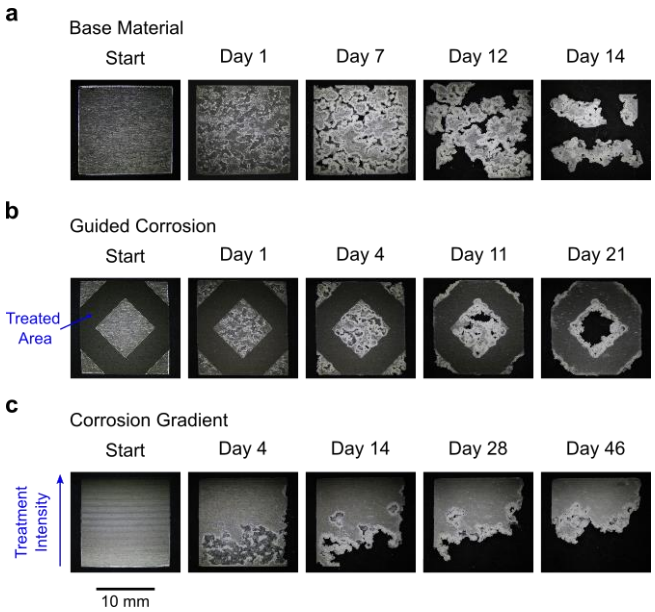

Figure 3. Proof of the "laser-guided corrosion control" concept. Degradation performance of untreated base material (a), material with T1 treatment over selected areas (b), restricting the degradation to untreated regions, and material with a gradual treatment (c), increasing the intensity from bottom to top (F from 0.5 to 1.8 J cm^{-2} and v from 73 to 10 mm s^{-1}), resulting in a corrosion gradient. Alloy used: AZ31. Refer to Supplementary Video 2 for video version.

Any application where a controlled degradation of a component is desirable may benefit from these ideas. As an example, anodes for cathodic protection of steel reinforcements in concrete

may be treated following the gradual strategy shown in Figure 3c, to control their degradation and increase the lifespan of the protection. Self-corrosion effects can be avoided, increasing the amount of anode material available to corrode when cathodic protection is required, as illustrated by **Figure 4**a.

As commented in the introduction, materials corrosion is exploited in the biomedical field for the development of biodegradable implants. In orthopedic applications, degradable magnesium implants are an interesting alternative to permanent metallic implants, with the benefits of avoiding the implant removal surgery and the stress shielding effects linked to stiffness mismatch between implant and bone tissues.[11,13] However, problems often arise linked to the fast degradation of magnesium in contact with body fluids. As an example, in Mg-based bone fracture fixation systems, localized degradation around screws and screws fixation holes is commonly reported *in vivo*,[15,45,46] compromising the mechanical stability required for bone tissue healing. The presented method may be useful to slow and control the degradation to maintain enough mechanical support. Figure 4b illustrates these ideas.

The value of the method for orthopedic applications was experimentally studied. Bone fracture fixation plates were prepared from the AZ31 magnesium alloy for subsequent treatment and immersion in the NaCl solution (see Experimental Section). As shown in Figure 4c, untreated plates suffered from severe degradation near the screw fixation holes. In contrast, the laser treatment effectively prevented this trend through the induced passivation process, which would extend the mechanical support for tissue healing in an *in vivo* application. In addition, the treatment can effectively control and drive the degradation towards specific areas of the part if required, as shown for the central area in Figure 4c. In addition, the capability of guiding the degradation behavior in a biomedical application was further evaluated by immersion tests in Dulbecco's modified Eagle's medium (DMEM) of samples with tailored treatments (Figure S8), showing the replicability of the results obtained in NaCl solution (Figure 3) in an environment much closer to the one found in an *in vivo* application.

The feasibility of the biomedical application of the presented method was further studied with cytotoxicity test. Extracts of untreated and T1-treated samples were prepared by immersion in Dulbecco's modified Eagle's medium (DMEM) for further incubation with L929 cells (see Experimental Section). XTT-based cell viability measurements show that the laser treatment reduces the toxicity levels found for the base material (Figure 4d, ANOVA test, p-value = 1.7×10^{-3}). A slower degradation of the treated samples in DMEM is likely the reason for the reduced toxicity,[47,48] as confirmed by inductively coupled plasma optical emission spectroscopy (ICP-OES) measurements of magnesium concentration in the extracts and a substantially lower precipitate formation on top of the treated samples (Figure S9). The decreased corrosion rates in cell medium foresee a reduction of other common problems arising from high corrosion rates of magnesium implants *in vivo* apart from premature mechanical failures, as local *pH* rise and formation of hydrogen cavities.[13–15,45,46]

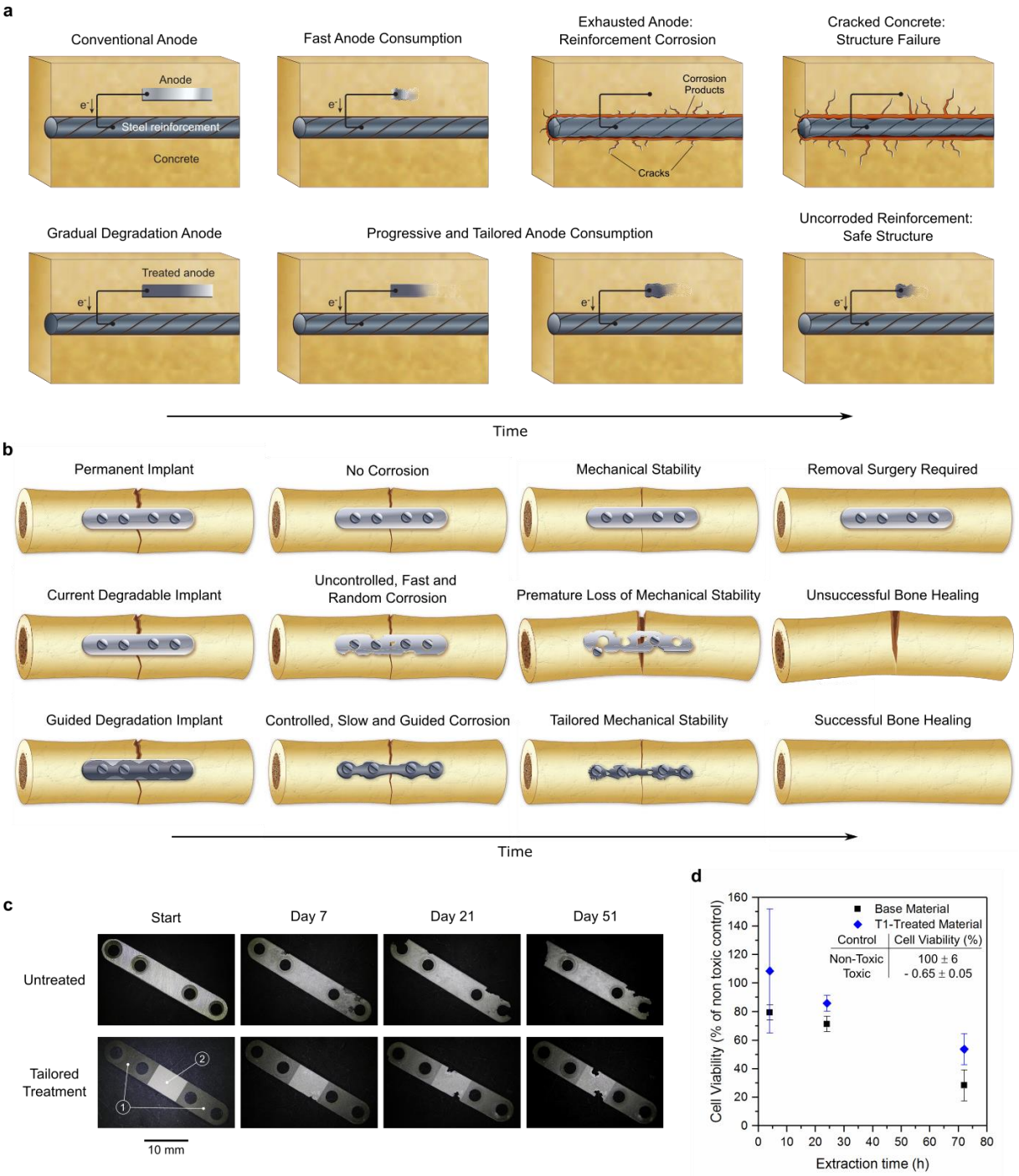

Figure 4. Applications. a) Application of the method for corrosion control of anodes for cathodic protection of steel reinforcements in concrete. b) Application of the method for biodegradable bone fixation plates. c) Macroscopic degradation performance of untreated and tailored-treated bone fracture fixation plates. Alloy used: AZ31. Regions in the latter were selectively treated as labelled: (1) $F = 1.8$ J cm^{-2}, $v = 10$ mm s^{-1}; (2) $F = 1.5$ J cm^{-2}, $v = 26$ mm s^{-1}. d) Cell viability values of extracts of base material and T1-treated samples for different extraction times.

In conclusion, the capability of guiding the corrosion process of Mg-alloys by means of a simple method based on direct laser irradiation has been demonstrated in this work. On the basis of a local control of the corrosion protection provided by the treatment, the degradation can be restricted to delimited regions of interest and can be driven towards specific directions by a

selective adjust of the overall corrosion rate in each region as shown. The presented results demonstrate the applicability of the method in the biomedical field, bringing about the possibility of designing implants with tailored degradation, adapted to different tissue requirements and environment conditions around different areas of the implant.[14,46,49] Other applications that profit from magnesium corrosion phenomena as new Mg batteries[2] or intelligent magnesium anodes for cathodic protection[4] may benefit from a local control of the process. Furthermore, a laser treatment can modify surface properties governing corrosion phenomena as microstructure, composition, topography or wettability on almost any material, opening the door to the application of the laser-guided corrosion control concept to other fields where a controlled material corrosion is desirable.

Experimental Section

Sample Preparation: The AZ31B magnesium alloy was employed in this study. Samples were mechanically cut to the size required for each processing and characterization technique from 1 mm thick foil (GoodFellow), received in the H24 temper (i.e. strain hardened by rolling and partially annealed afterwards).[34] Additional experiments were performed with equally sized samples from pure Mg foil, AZ91D as-cast ingot and AZ61 extruded rod (GoodFellow). The nominal composition of all materials is included in Table S1. Both before and after the laser treatment, all samples were rinsed with ethanol and exposed to a blast of dry air to remove any solid remainder that could affect either the laser irradiation process or the following tests and measurements.

Laser Processing: Direct laser irradiation was performed using a Nd:YVO_4 diode end-pumped laser (Rofin) emitting in pulsed regime with a pulse width of 20 ns and a wavelength of λ = 1064 nm**.** The laser beam (TEM_{00} mode and quality factor $M^2 < 1.3$) was guided by two galvo mirrors mounted on an XY scanning head and focused onto the surface of the samples with an F-Theta lens of focal length f_L =211 mm from a collimated $1/e^2$ diameter $\emptyset_{LENS}$ = 2.5 mm. With this set up, a spot size of 150 μm was measured, confirming the Gaussian beam optics estimation (approx. 149 μm) according to[50] $\emptyset_{SPOT} = 4M^2 \lambda f_L [\pi \emptyset_{LENS}]^{-1}$.

The surface of the samples was treated following a pattern of parallel scanning lines with a hatching distance of 0.1 mm. The processing parameters varied during the experiments were the pulse fluence F, ranging between [0, 1.8] J cm^{-2}, and the scanning speed v, ranging between [10,100] mm s^{-1}. The pulse frequency was kept constant at 20 kHz.

Experiments comparing air and argon atmospheres were performed by supplying to the processing area a total gas flow rate of 90 l/min through two lateral nozzles with individual cross section of 2 × 40 mm^2.

For a qualitative explanation of the thermal processes undergone by the material during the laser irradiation, the thermal relaxation time t_D was estimated from the one-dimensional

diffusion equation, $l_D = (D\ t_D)^{1/2}$. Here D represents the thermal diffusivity of the material, about 5×10^{-5} m^2 s^{-1} for AZ31B[34], and l_D represents the diffusion length, approximated with the beam radius (75 μm) as the characteristic length of the process.[20] That gives an estimation of 10^{-4} s as an order of magnitude for t_D.

Surface Topography Measurements: Surface topography was quantitatively characterized by focus variation optical profilometry (Alicona IF). According to definitions in ISO 25178, the arithmetic mean height of the surface S_a (μm) and the ratio of the increment in the interfacial area to the area of a perfectly flat surface S_{dr} (%) were registered for each analyzed sample. Note that S_{dr} is 0% for a perfectly flat surface, so for a given S_{dr} value, the actual surface area is a factor of $(1 + S_{dr}/100)$ higher than the one of a perfectly flat surface. A total area of 4 mm^2 was analyzed for each sample, covering the width of 20 laser scanning lines.

Surface Wettability Measurements: Surface wettability was evaluated via contact angle θ (°) measurements using the sessile drop method. According to recommendations in European standard EN 828:2013, 2 μl drops of Milli-Q distilled water were deposited on the samples with a micropipette and the contact angle was assessed with an electronic goniometer (Ossila Ltd.). At least 5 measurements were registered for each sample, reporting the mean and standard deviation.

Microstructural Characterization: Microstructure analyses were performed in cross-section view. To ensure an accurate identification of the microstructural features, the samples were cold mounted in epoxy resin to avoid recrystallization effects and were polished using water-free lubricants to prevent oxidation, with a final abrasive agent size of 0.05 μm. Whenever required, the samples were chemically etched in a solution of 75 ml ethylene glycol, 24 ml distilled water and 1 ml nitric acid for 45 s. Subsequent analyses were performed by SEM (FEI Quanta 200). The compositional differences and quantifications were analyzed by backscattered electrons and energy-dispersive X-ray spectroscopy (EDS). Atomic ratios were calculated from EDS

quantifications with at least 9 measurements for each ratio and material, reporting the mean and standard deviation. The crystallographic orientations were characterized by electron backscatter diffraction (EBSD, FEI Helios NanoLabTM DualBeamTM 600i equipped with an HKL NordlysNano EBSD detector and both Aztec and Channel 5.0 data acquisition and analysis software packages). The grain size was measured via the line intercept method. At least 200 grains were analyzed for each material. Reported values are the mean and the range enclosing 2/3 of the measurements.

Surface Chemistry Characterization X-ray photoelectron spectroscopy (XPS) analyses were performed with a Thermo Scientific K-Alpha ESCA instrument with Al Kα X-ray source at 1486.6 eV. Survey spectra were registered with a 100 eV pass energy, collecting the photoelectrons at a take-off angle of 90° from the sample in constant analyzer energy mode (CAE). Before the analysis, samples were sputter-cleaned with 500 eV energy argon ions during 60 s, obtaining a partial removal of the adventitious carbon contamination with the aim of improving the signal to noise ratio for the metal species and evaluate atomic ratios for elements of interest. Binding energy was referenced by setting the lower adventitious C 1s hydrocarbon photo peak at 285.0 eV.

Immersion Tests: The overall corrosion performance was evaluated via immersion test in normal saline solution (NaCl 9 g l^{-1}). Samples of 11 × 11 × 1 mm^3 were immersed in individual containers with a mass to volume ratio of 5.4 mg ml^{-1}. The tests were carried out under static conditions at 20 °C for immersion times of 1, 3, 7, 14 and 21 days. At each time point, the *pH* was measured with a *pH* probe, and the specimens were removed and cleaned with ethanol and dry air. Optical microscopy was employed to analyze the overall corrosion progression. Mass loss was assessed with a gravimetric balance (Nahita). The ratio between the mass of the specimen after and before the immersion was finally registered for each specimen. To confirm the mass loss results, the magnesium concentration in the remaining immersion solutions was measured by inductively coupled plasma optical emission spectroscopy (ICP-OES,

PerkinElmer). Prior to this, to ensure the dissolution of any magnesium compound that could have precipitated, the immersion solutions were diluted in 2% nitric acid to a ratio of 1/10. For both the untreated base material and the 4 different treatments evaluated, 3 independent samples were tested for each immersion time. The reported values are the mean and standard deviation of those three replicates. The degradation rates were estimated by linear fitting of the evolution of mass loss values over time.

Real Time Corrosion Monitoring: The corrosion process of the samples in the NaCl solution was monitored in real time in order to assess the qualitative aspects of the corrosion process with more detail within the first 24 hours of immersion. The process was monitored in top view with an optical microscope equipped with a digital camera (Canon) recording at 29 fps with a resolution of 1280 × 790 px.

EIS Measurements: Electrochemical impedance spectroscopy (EIS) measurements were performed employing an electrochemical cell in three-electrode arrangement, with the studied sample acting as the working electrode, a platinum counter electrode and a Ag/AgCl pseudo-reference electrode. NaCl solution (0.5 M) was used as electrolyte. The high hydrophilicity of the samples prevented an acceptable operation with the usual solution confinement procedures (O-rings or silicone sealing). This issue was solved by immobilization of the electrolyte in a cellulose cylinder cast in a glass tube (approximately 5 cm long). In this way, the capillary pressure in the cellulose cylinder was able to limit the tendency of the liquid to spread over the sample's surface, and a nominal active surface of 0.5 cm^2 was defined. The experiments were conducted using a potentiostat (Autolab) with a frequency response analyzer (FRA) module. The impedance spectra were obtained at the corrosion potential, ranging from 10^6 to 10^{-1} Hz with seven frequency data points per decade logarithmically distributed. The measurements were performed under galvanostatic control at $I = (0 \pm \Delta I)$, with ΔI selected for a resulting polarization voltage amplitude close to 5 mV rms. The measurements were performed at

specific times within 1 hour of immersion. All the tests were conducted at 20 °C and open to the atmosphere.

Regarding the fitting procedures (see equivalent circuit in Figure 2c), the inductive loops in the low frequency range linked to changes in surface coverage of adsorbed intermediates were modeled by an inductance L with a series resistance R_L.[28–30] The capacitive loops in the frequency range around 10 Hz were fitted by a finite-length diffusion term Z_D modeled as[27] $Z_D = R_D \tanh[(j\omega \tau_D)^{1/2})]/(j\omega \tau_D)^{1/2}$. Here, R_D accounts for the diffusion resistance, τ_D corresponds to the time constant associated to the transport process, ω is the angular frequency and j the imaginary unit.

As described in the main text, the capacitive loops around 100 Hz – 1 kHz were fitted by the time constant associated to the interfacial properties $R_{CT}C_{DL}$. The capacitive features at the high frequency end of the spectra were fitted by the time constant associated to the dielectric properties of the protective layer R_FC_F. For both time constants, Cole-Cole type dispersion parameters α_i were introduced to account for deviations from ideal capacitive behavior ($\alpha_i = 1$) due to heterogeneities in thickness and/or composition along the normal direction.[51,52] The impedance terms were then modeled as $Z_i = Z_{IIi}/[1+(j\omega Z_{IIi}C_i)^{\alpha_i}]$, where $_{i = DL, F}$ and $Z_{//i}$ the equivalent impedance in parallel with C_i.

The overall corrosion resistance of the samples was characterized by the so-called polarization resistance R_P, which is inversely proportional to the corrosion rate[30]. This resistance was estimated by the DC equivalent of the impedance spectrum without accounting for the electrolyte resistance R_E. Therefore, in terms of the fitted resistance components, $R_P = R_F + [(R_{CT} + R_D)^{-1} + R_L^{-1}]^{-1}$ (see equivalent circuit in Figure 2c).

Bone Fracture Fixation Plates: Plates were mechanically prepared from the original AZ31 foil. Final dimensions are 30 mm length, 5 mm width and 1 mm thickness. 4 screw fixation holes

with 2.4 mm inner diameter were drilled in each plate. The degradation of untreated and treated plates was tested by immersion in normal saline solution (NaCl 9 g l^{-1}).

Cytotoxicity Tests: Cytotoxicity tests were performed via indirect contact through incubation of cells with liquid extracts of the samples. Samples were first sterilized by immersion in isopropanol and UV exposure. Extracts of the samples were prepared by immersion in Dulbecco's modified Eagle's medium (DMEM, Gibco) supplemented with GlutaMAX, 10% fetal bovine serum, 1% penicillin/streptomycin and 0.1% amphotericin B. Samples of 9 × 9 × 1 mm^3 were immersed with a mass to volume ratio of 0.032 g ml^{-1} for 4, 24 and 72 hours at 37 °C in a CO_2 incubator. After the specific extraction time, the extracts were centrifuged at 4000 rpm during 5 minutes and filtered through a 0.22 μm pore size filter. Extracts composition was characterized by ICP-OES of the aliquots. L929 cells were seeded in 96-well cell culture plates at a density of 3000 cells per well and 100 μl of cell medium. After 24 hours, the cell medium was replaced by an equal amount of the corresponding extracts and further incubated for 3 days. Cytotoxicity was then tested by XTT assay. To avoid reported interactions between magnesium and tetrazolium-based tests,[47,53] before addition of XTT reagents the extracts were removed and replaced by 100 μl of cell medium. Thereafter, 50 ml of XTT solution was added to each well. After 2 hours of further incubation, the absorbance at 465 nm was measured, with 630 nm as reference wavelength. Cell medium without cells was used as blank reference for absorbance measurements. Cells incubated in cell medium and in cell medium with 50% DMSO were adopted as non-toxic and toxic controls respectively. 3 replicates were tested for each material and extraction time combination. The reported values are the mean and standard deviation of those three replicates.

Supporting Information
Supporting Information is available from the Wiley Online Library or from the author.

Acknowledgements
The authors wish to thank the technical staff from Electron Microscopy, Nanotechnology and

Surface Analysis and Food Security groups at CACTI (University of Vigo, Vigo) for their help with sample characterization, I. Pazos (University of Vigo, Vigo) for her assistance with SEM analyses, Dr. C. Serra (University of Vigo, Vigo) for her assistance with XPS analyses, T. McFarlane (Imperial College, London) for her advice on cytotoxicity tests methodology, the technical staff from Cell Culture Unit (IISGS, Vigo) for their assistance with cytotoxicity tests and Dr. C. Conde (University Hospital Complex, Vigo) for his advice on osteosynthesis application. This work was partially supported by EU research project Bluehuman (EAPA_151/2016 Interreg Atlantic Area), by the Government of Spain [RTI2018-095490-J-I00 (MCIU/AEI/FEDER, UE), FPU16/05492, PID2019-111285RB-I00], by Xunta de Galicia (ED431C 2019/23, ED481D 2017/010, ED481B 2016/047-0, ED431B2017/65-GPC) and by the Madrid region (S2018/NMT-4381-MAT4.0-CM).

Received: ((will be filled in by the editorial staff))
Revised: ((will be filled in by the editorial staff))
Published online: ((will be filled in by the editorial staff))

Conflict of Interest
The authors declare no conflict of interest.

References

[1] D. Lin, Y. Liu, Y. Cui, *Nat. Nanotechnol.* **2017**, *12*, 194.

[2] M. Li, J. Lu, X. Ji, Y. Li, Y. Shao, Z. Chen, C. Zhong, K. Amine, *Nat. Rev. Mater.* **2020**, *5*, 276.

[3] A. Byrne, B. Norton, N. Holmes, *Mag. Concr. Res.* **2016**, *68*, 664.

[4] L. Yan, G. L. Song, D. Zheng, *Corros. Sci.* **2019**, *155*, 13.

[5] L. S. Nair, C. T. Laurencin, *Prog. Polym. Sci.* **2007**, *32*, 762.

[6] Y. F. Zheng, X. N. Gu, F. Witte, *Mater. Sci. Eng. R Reports* **2014**, *77*, 1.

[7] J. R. Jones, *Acta Biomater.* **2015**, *23*, S53.

[8] B. N. Popov, *Corrosion Engineering: Principles and Solved Problems*, Elsevier, Amsterdam, **2015**.

[9] R. A. McCauley, *Corrosion of Ceramic Materials*, CRC Press, Boca Raton, **2016**.

[10] M. Kutz, *Handbook of Environmental Degradation of Materials*, Elsevier, Amsterdam, **2018**.

[11] M. P. Staiger, A. M. Pietak, J. Huadmai, G. Dias, *Biomaterials* **2006**, *27*, 1728.

[12] F. Witte, N. Hort, C. Vogt, S. Cohen, K. U. Kainer, R. Willumeit, F. Feyerabend, *Curr. Opin. Solid State Mater. Sci.* **2008**, *12*, 63.

[13] D. Zhao, F. Witte, F. Lu, J. Wang, J. Li, L. Qin, *Biomaterials* **2017**, *112*, 287.

[14] J. Walker, S. Shadanbaz, T. B. F. Woodfield, M. P. Staiger, G. J. Dias, *J. Biomed. Mater. Res. - Part B Appl. Biomater.* **2014**, *102*, 1316.

[15] T. Imwinkelried, S. Beck, B. Schaller, *Mater. Sci. Eng. C* **2020**, *108*, 110389.

[16] J. Dutta Majumdar, R. Galun, B. L. Mordike, I. Manna, *Mater. Sci. Eng. A* **2003**, *361*, 119.

[17] A. E. Coy, F. Viejo, F. J. Garcia-Garcia, Z. Liu, P. Skeldon, G. E. Thompson, *Corros. Sci.* **2010**, *52*, 387.

[18] B. N. Chichkov, C. Momma, S. Nolte, F. von Alvensleben, A. Tünnermann, *Appl. Phys. A Mater. Sci. Process.* **1996**, *63*, 109.

[19] A. D. Zweig, *J. Appl. Phys.* **1991**, *70*, 1684.

[20] M. Stafe, C. Negutu, I. M. Popescu, *Appl. Surf. Sci.* **2007**, *253*, 6353.

[21] G. L. Song, A. Atrens, *Adv. Eng. Mater.* **1999**, *1*, 11.

[22] A. Atrens, G. L. Song, M. Liu, Z. Shi, F. Cao, M. S. Dargusch, *Adv. Eng. Mater.* **2015**, *17*, 400.

[23] M. Esmaily, J. E. Svensson, S. Fajardo, N. Birbilis, G. S. Frankel, S. Virtanen, R. Arrabal, S. Thomas, L. G. Johansson, *Prog. Mater. Sci.* **2017**, *89*, 92.

[24] *CRC Handbook of Chemistry and Physics*, CRC Press, Boca Raton, **2004**.

[25] D. Quéré, *Annu. Rev. Mater. Res.* **2008**, *38*, 71.

[26] P. Pou, J. del Val, A. Riveiro, R. Comesaña, F. Arias-González, F. Lusquiños, M. Bountinguiza, F. Quintero, J. Pou, *Appl. Surf. Sci.* **2019**, *475*, 896.

[27] M. E. Orazem, B. Tribollet, *Electrochemical Impedance Spectroscopy*, John Wiley & Sons, Inc., Hoboken, NJ, **2008**.

[28] G. Baril, G. Galicia, C. Deslouis, N. Pébère, B. Tribollet, V. Vivier, *J. Electrochem. Soc.* **2007**, *154*, C108.

[29] M. P. Gomes, I. Costa, N. Pébère, J. L. Rossi, B. Tribollet, V. Vivier, *Electrochim. Acta* **2019**, *306*, 61.

[30] A. D. King, N. Birbilis, J. R. Scully, *Electrochim. Acta* **2014**, *121*, 394.

[31] G. Song, A. Atrens, D. St. John, X. Wu, J. Nairn, *Corros. Sci.* **1997**, *39*, 1981.

[32] C. M. Abreu, M. J. Cristóbal, R. Losada, X. R. Nóvoa, G. Pena, M. C. Pérez, *J. Electroanal. Chem.* **2004**, *572*, 335.

[33] B. Guitián, X. R. Nóvoa, A. Pintos, *Electrochim. Acta* **2019**, *304*, 428.

[34] M. M. Avedesian, H. Baker, Eds. , *ASM Specialty Handbook. Magnesium and Magnesium Alloys*, ASM International, **1999**.

[35] I. Ulacia, N. V. Dudamell, F. Gálvez, S. Yi, M. T. Pérez-Prado, I. Hurtado, *Acta Mater.* **2010**, *58*, 2988.

[36] G. L. Song, R. Mishra, Z. Xu, *Electrochem. commun.* **2010**, *12*, 1009.

[37] A. K. Mondal, S. Kumar, C. Blawert, N. B. Dahotre, *Surf. Coatings Technol.* **2008**, *202*, 3187.

[38] C. Liu, J. Liang, J. Zhou, L. Wang, Q. Li, *Appl. Surf. Sci.* **2015**, *343*, 133.

[39] M. Jönsson, D. Thierry, N. LeBozec, *Corros. Sci.* **2006**, *48*, 1193.

[40] M. A. Melia, P. Steiner, N. Birbilis, J. M. Fitz-Gerald, J. R. Scully, *Corrosion* **2016**, *72*, 95.

[41] K. D. Ralston, N. Birbilis, *CORROSION* **2010**, *66*, 075005.

[42] G. L. Makar, *J. Electrochem. Soc.* **1992**, *139*, 47.

[43] J. M. Fishburn, M. J. Withford, D. W. Coutts, J. A. Piper, *Appl. Surf. Sci.* **2006**, *252*, 5182.

[44] J. M. Fishburn, M. J. Withford, D. W. Coutts, J. A. Piper, *Appl. Surf. Sci.* **2006**, *253*, 662.

[45] B. Schaller, N. Saulacic, T. Imwinkelried, S. Beck, E. W. Y. Liu, J. Gralla, K. Nakahara, W. Hofstetter, T. Iizuka, *J. Cranio-Maxillofacial Surg.* **2016**, *44*, 309.

[46] H. Naujokat, J. M. Seitz, Y. Açil, T. Damm, I. Möller, A. Gülses, J. Wiltfang, *Acta Biomater.* **2017**, *62*, 434.

[47] J. Fischer, D. Pröfrock, N. Hort, R. Willumeit, F. Feyerabend, *Mater. Sci. Eng. B Solid-State Mater. Adv. Technol.* **2011**, *176*, 1773.

[48] J. Wang, F. Witte, T. Xi, Y. Zheng, K. Yang, Y. Yang, D. Zhao, J. Meng, Y. Li, W. Li, K. Chan, L. Qin, *Acta Biomater.* **2015**, *21*, 237.

[49] J. Gonzalez, R. Q. Hou, E. P. S. Nidadavolu, R. Willumeit-Römer, F. Feyerabend, *Bioact. Mater.* **2018**, *3*, 174.

[50] W. M. Steen, J. Mazumder, *Laser Material Processing*, Springer London, London, **2010**.

[51] K. S. Cole, R. H. Cole, *J. Chem. Phys.* **1941**, *9*, 341.

[52] M. E. Orazem, I. Frateur, B. Tribollet, V. Vivier, S. Marcelin, N. Pébère, A. L. Bunge, E. A. White, D. P. Riemer, M. Musiani, *J. Electrochem. Soc.* **2013**, *160*, C215.

[53] O. Jung, R. Smeets, D. Porchetta, A. Kopp, C. Ptock, U. Müller, M. Heiland, M. Schwade, B. Behr, N. Kröger, L. Kluwe, H. Hanken, P. Hartjen, *Acta Biomater.* **2015**, *23*, 354.

Table of Contents

Laser-guided corrosion control: a new approach to tailor the degradation of Mg-alloys

*Pablo Pou-Álvarez, Antonio Riveiro, Xosé Ramón Nóvoa, Xueze Jin, Jesús del Val, Rafael Comesaña, Mohamed Boutinguiza, Fernando Lusquiños, Julian R. Jones, María Teresa Pérez-Prado, and Juan Pou**

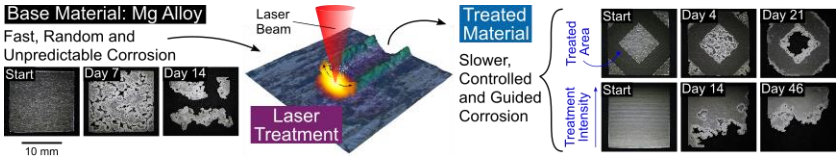

A novel concept of controlling and guiding the corrosion process of a material through a laser treatment is presented. After the treatment, the degradation is no longer random and unpredictable, but progresses towards the designed regions and directions. Applications like batteries, biodegradable implants or cathodic protection systems may benefit from such a controlled and tailored corrosion.